OPEN ACCESS
JOURNAL OF ADVANCED DIELECTRICS
Vol. 14, No. 1 (2024) 2350022 (8 pages)

DOI: 10.1142/S2010135X23500224

Substitution of Pb with $(Li_{1/2}Bi_{1/2})$ in $PbZrO_3$-based antiferroelectric ceramics

Binzhi Liu, Anand P. S. Gaur, Jun Cui and Xiaoli Tan*
Department of Materials Science and Engineering
Iowa State University, Ames, IA 50011, USA
*xtan@iastate.edu

Received 11 August 2023; Revised 13 September 2023; Accepted 7 October 2023; Published 31 October 2023

$PbZrO_3$-based antiferroelectric (AFE) ceramics are promising dielectrics for high-energy-density capacitors due to their reversible phase transitions during charge–discharge cycles. In this work, a new composition series, $[Pb_{0.93-x}La_{0.02}(Li_{1/2}Bi_{1/2})_xSr_{0.04}][Zr_{0.57}Sn_{0.34}Ti_{0.09}]O_3$, with Li^+ and Bi^{3+} substitution of Pb^{2+} at $x = 0, 0.04, 0.08, 0.12, 0.16$ is investigated for the microstructure evolution, ferroelectric (FE) and dielectric properties. It is found that Li^+ and Bi^{3+} substitution can significantly reduce the sintering temperature and simultaneously enhance the dielectric breakdown strength. An ultrahigh energy efficiency (94.0%) and a large energy density ($3.22\,J/cm^3$) are achieved in the composition of $x = 0.12$ with a low sintering temperature (1075°C).

Keywords: $PbZrO_3$-based antiferroelectrics; Li+Bi substitution; energy storage; energy efficiency.

1. Introduction

Antiferroelectric (AFE) ceramics have revived much attention in recent years because of many potential applications, such as high-energy-density capacitors, high-strain actuators, electrocaloric devices, infrared detectors, etc.[1–4] They are particularly promising for the next-generation energy-storage capacitors due to their extremely low-remanent polarization, relatively high permittivity, high power density and ultrafast charge/discharge rate.[2,5–7] All these applications capitalize on the electric field-induced AFE-to-ferroelectric (FE) phase transition. In the macroscopic polarization measurement, the reversible phase transitions are manifested as double hysteresis loops, from which the forward critical field E_F and the reverse critical field E_A can be directly read.

Although extensive efforts have been spent searching for lead-free AFE materials,[8–14] $PbZrO_3$-based AFEs still remain competitive because of their superb properties.[2,7,15–22] $PbZrO_3$ is the prototype AFE, but its low dielectric strength at room temperature, practically lower than the critical field E_F, limits its application in devices. Another shortcoming of $PbZrO_3$-based ceramics is their large electric hysteresis during the phase transition process, where the dissipated energy degrades the performance of electric devices drastically. In the literature, the recoverable energy density during discharge is denoted as W_{rec}; the dissipated energy density due to electric hysteresis is denoted as W_{loss}, and the total stored energy density during charging is denoted as W_{st}. Analytically, these energy properties can be expressed as follows:

$$W_{st} = \int_0^{P_{max}} EdP, \tag{1}$$

$$W_{rec} = \int_{P_r}^{P_{max}} EdP, \tag{2}$$

$$W_{loss} = W_{st} - W_{rec}, \tag{3}$$

$$\eta = \frac{W_{rec}}{W_{st}}, \tag{4}$$

where P_{max} is the maximum polarization, P_r is the remanent polarization, and η is the charge–discharge energy efficiency.

The sintering process at high temperature is an essential step in ceramic fabrication, where the energy consumption accounts for a large portion of manufacturing cost. To reduce the sintering temperature, sintering aids, such as Bi_2O_3, are often used.[23–27] It is expected that the low melting point of Bi_2O_3 will assist the sintering process in achieving a high density at a reduced sintering temperature. On the other hand, reduced sintering temperatures may limit the full growth of grains, resulting in ceramics with a smaller grain size. According to the empirical relationship:

$$BDS \propto d^{-a}, \tag{5}$$

where BDS refers to the dielectric breakdown strength and d is the grain size, a ranges from 0.2 to 0.4,[28–30] a smaller grain size of dielectric ceramics correlates with a higher breakdown strength.

Typically, a relaxor has complex compositions with multiple cations of different valences sharing the same lattice site. The random occupancy of these cations in the lattice disrupts the long-range FE order, which creates easily polarized polar nanoregions, leading to a nearly zero electric hysteresis.[31–33] Parallel to this phenomenon, the "relaxor AFE" concept has been proposed.[19,34–36] The disruption of the AFE long-range order results in the formation of nanometer-sized AFE

domains, making it easier for the antiparallel cation displacement to flip with reduced hysteresis. Furthermore, A-site vacancies in perovskite oxides also enhance the relaxor behavior.[37,38] The "relaxor AFE" concept has successfully led to the development of a series of AFE compositions with reduced electric hysteresis and enhanced energy efficiency.[19]

Various chemical modification schemes have been explored to adjust critical fields and address electric hysteresis in $PbZrO_3$-based AFEs, such as La^{3+}, Ba^{2+}, Sr^{2+} substitution for Pb^{2+} on the A-site and Sn^{4+}, Ti^{4+} substitution for Zr^{4+} on the B-site.[39–42] However, the energy efficiency, η, of most $PbZrO_3$-based AFE materials still remains mediocre in the range of 60– 80%. In this work, Li^+ and Bi^{3+} are introduced in an equal molar ratio to a base AFE composition, $(Pb_{0.93}La_{0.02}Sr_{0.04})(Zr_{0.57}Sn_{0.34}Ti_{0.09})O_3$, as a sintering aid and to substitute Pb^{2+} on the A-site. Multiple benefits, including reduced sintering temperature, improved breakdown strength and enhanced energy efficiency, are simultaneously realized.

2. Experimental Procedure

The synthesis of $[Pb_{0.93-x}La_{0.02}(Li_{1/2}Bi_{1/2})_xSr_{0.04}][Zr_{0.57}Sn_{0.34}Ti_{0.09}]O_3$ ceramics (Denoted as LB100x hereafter with $x = 0$, 0.04, 0.08, 0.12, 0.16) is carried out using the solid-state reaction method. High-purity raw powders (>99.9%) of PbO, La_2O_3, Li_2CO_3, Bi_2O_3, $SrCO_3$, ZrO_2, SnO_2 and TiO_2 are baked to remove the moisture before mixing. Because of the evaporation nature of PbO during high-temperature processing, an excess of 5 wt.% PbO is added to preserve the designed stoichiometry. The dry powder is batched according to the chemical formula and mixed in ethanol on a vibratory mill for 6 h with zirconia media. The mixed slurry is dried for 24 h, and the powder is subsequently calcined at 935°C for 4 h, after which the calcined powder is re-milled for another 6 h and dried for 24 h. The dry powder is mixed with 10 wt.% polyvinyl alcohol binder and uniaxially pressed into green pellets at a pressure of 150 MPa. The pellets are de-bindered at 600°C for 3 h and then sintered at temperatures in the range of 1075–1350°C. During sintering, the pellets are buried in the calcined powder of the same composition to minimize the evaporation loss of PbO. A double crucible setup is applied to further reduce the PbO loss and maintain the desired composition stoichiometry during sintering.

X-ray diffraction (XRD) is performed to analyze the crystal structure and phase purity of the sintered ceramics on a Siemens D500 X-ray diffractometer using the Cu-Kα radiation in a 2θ range from 20° to 80°. The fracture surface of the ceramics is examined with FEI Inspect 50 scanning electron microscope (SEM) to reveal the grain morphology and size. To characterize the domain structure within the grains, a transmission electron microscope (FEI Titan Themis) is used. TEM samples are prepared using traditional procedures, including polishing, ultrasonic cutting, dimpling and ion-milling.

To characterize the dielectric and FE properties, ceramic pellets are polished down to ~ 0.25 mm thickness and sputter-coated Pd films (4 mm diameter) as electrodes. The polarization versus electric field loops are measured at room temperature at a frequency of 1 Hz using a standardized FE test system (Precision LC II, Radiant Technologies). The dielectric constant and loss tangent of the ceramics are measured using a Novocontrol system at a heating rate of 1°C/min at 1 kHz frequency.

3. Results and Discussion

3.1. *Structure of the ceramics*

Ceramic of each composition was sintered at several temperatures and the energy storage properties were characterized. The optimal sintering temperature was then identified and found to gradually decrease as the doping level increases from $x = 0$ to $x = 0.12$. The sintered ceramic pellets of all compositions exhibit a relative density > 95% at their optimal sintering temperatures, which reduced from 1350°C for the base composition to 1075°C for the composition of $x = 0.12$. The XRD patterns of the LB100x series ceramics sintered at optimal temperatures are shown in Figs. 1(a) and 1(b). The sintered ceramics of compositions $x = 0$ through 0.12 are in perovskite phase with tetragonal distortions; for the high-dopant composition $x = 0.16$ sintered at 1075°C, a secondary phase, $La_2Sn_2O_7$, is present. $La_2Sn_2O_7$ might be an intermediate phase during the formation of the final perovskite phase at the low sintering temperature of 1075°C. As a comparison experiment, $x = 0.16$ is also

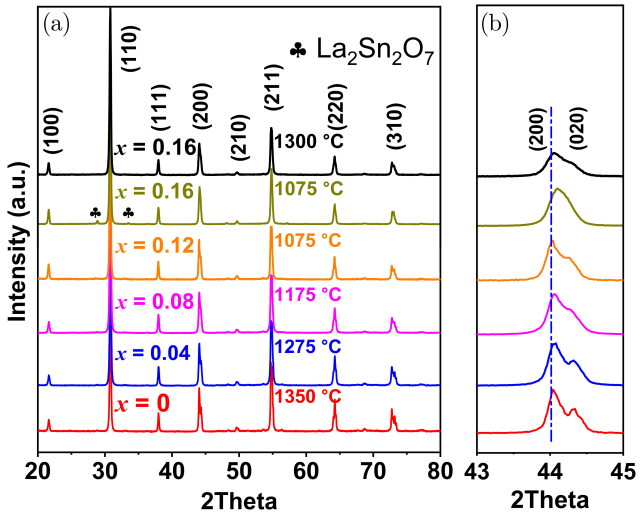

Fig. 1. (a) X-ray diffraction spectra of the LB100x ($x = 0$, 0.04, 0.08, 0.12, 0.16) sintered ceramics with peaks indexed on the basis of a pseudocubic unit cell. (b) The enlarged view from 43 to 45° of 2θ. The ceramic of $x = 0.16$ is displayed for its spectra collected on pellets sintered at low (1075 °C) and high (1300 °C) temperatures.

sintered at a high temperature of 1300°C, and XRD is performed. As expected, the $La_2Sn_2O_7$ impurity phase disappears. Figure 1(b) provides a close view of the XRD pattern in the 2θ range from 43° to 45°, where the (200)/(020) split peaks shift to the higher 2θ angle region.[19,38] This peak shift is likely due to the smaller radii of A-site substitutions [Li^+ (1.05 Å, this value is estimated by extrapolation for a 12-coordinated Li^+), Bi^{3+} (1.35 Å)] compared to those in the base composition [Pb^{2+} (1.49 Å), Sr^{2+} (1.44 Å), La^{3+} (1.36 Å)].[43] The incorporated smaller ions lead to a decrease in the interplanar spacings because of the more compact unit cell, which results in the XRD peaks shifting to higher 2θ angles. The peak shift is accompanied by the merging of the doublet, which is a sign of the reduction of tetragonality, and the gradual transition of the crystal structure to the cubic phase as the $(Li_{1/2}Bi_{1/2})$-substitution increases. It is interesting to note that the splitting of (200)/(020) peak in the composition $x = 0.16$ does not occur at the low-sintering temperature of 1075°C but can be resolved when sintered at 1300°C, indicating an almost cubic structure in the pellet sintered at 1075°C.

Figure 2 shows the representative SEM micrographs of the fracture surface of as-sintered ceramics. Intergranular fracture features are dominant and the high density of ceramics is also verified. The grain size is quantified with the line intercept method following appropriate statistical methods, and over 300 grains are measured for each composition. The distribution of grain size is overlaid on the SEM micrographs. The average values are plotted in Fig. 3 and listed in Table 1 together with sintering temperatures and electrical properties. The grain size reduces significantly with the increase of $(Li_{1/2}Bi_{1/2})$-substitution. The grain size of the base composition is 4.98 μm, and whilst that of the $x = 0.16$ composition

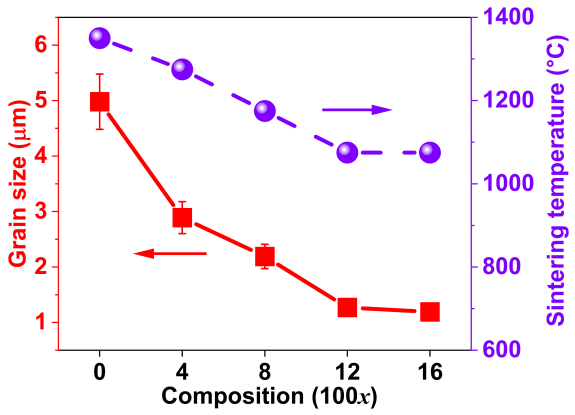

Fig. 3. Sintering temperatures of LB100x ceramic series and the resulting grain size.

is reduced to 1.19 μm. In the substitution range of $x \leq 0.12$, the grains display a strong faceting tendency. In the composition $x = 0.16$, some small spherical particles in between the large faceted grains are observed. They are very likely to be the secondary phase $La_2Sn_2O_7$.

Figure 4 showcases TEM bright-field micrographs of $x = 0$ and $x = 0.12$, along with their corresponding electron diffraction patterns. In Fig. 4(a), a large $[001]_c$-oriented grain of the base composition is imaged. Characteristic AFE domains in the checkerboard pattern are evident. Incommensurate modulations in the form of fringes are clearly discernible. The areas a_2 and a_3 are located in separate 90° AFE domains, while area a_1 is sitting across the AFE domain wall. Correspondingly, the electron diffraction patterns display two sets of satellite diffraction spots along orthogonal directions.[44] Incommensurate modulations in $PbZrO_3$-based

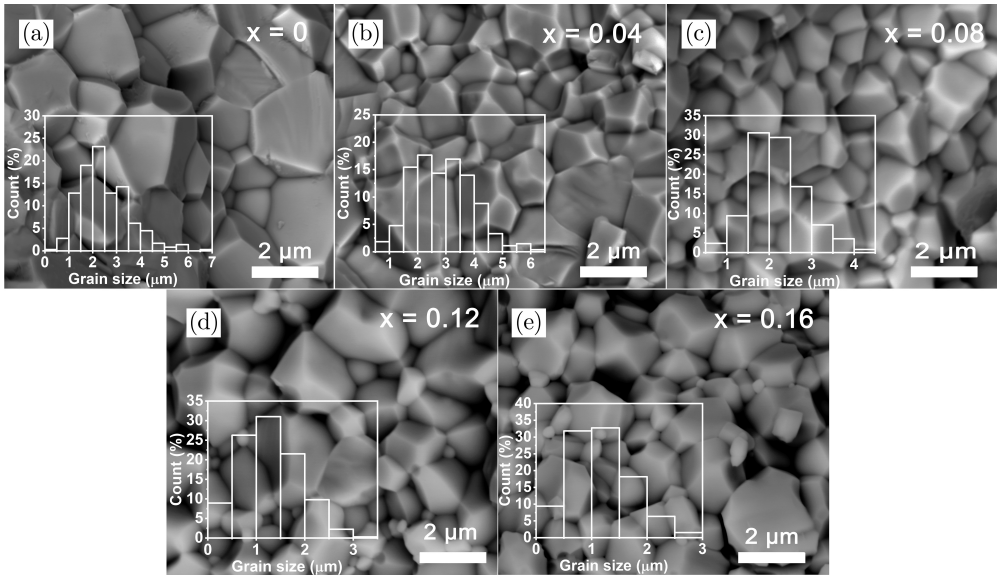

Fig. 2. SEM micrographs of the fracture surface of LB100x ceramics. (a) $x = 0$, (b) $x = 0.04$, (c) $x = 0.08$, (d) $x = 0.12$, (e) $x = 0.16$. The grain size analysis is overlaid on the micrograph.

Table 1. Sintering temperature, grain size, recoverable energy density W_{rec}, energy efficiency η, temperature at dielectric peak T_m, dielectric relaxation parameters γ and δ of the LB100x ceramics.

Composition 100x	T_{sinter} °C	Grain size μm	W_{rec} J/cm^3	η %	T_m °C	γ —	δ —
0	1350	4.98	3.56	90.3	153	1.53	44.85
4	1275	2.89	3.42	92.6	149	1.48	46.37
8	1175	2.19	3.23	90.4	143	1.74	97.85
12	1075	1.27	3.22	94.0	140	1.84	128.76
16	1075	1.19	2.58	90.0	142	1.82	119.87

ceramics are characterized by the presence of satellite diffraction spots that can be indexed as $1/n\{110\}$. The satellite spots are round and sharp in the base composition ($x = 0$) and the value of n is determined to be 6.98 for the selected area diffraction pattern in Fig. 4(a_2), and 7.00 for the diffraction pattern in Fig. 4(a_3). These values are consistent with previous reports.[39,44]

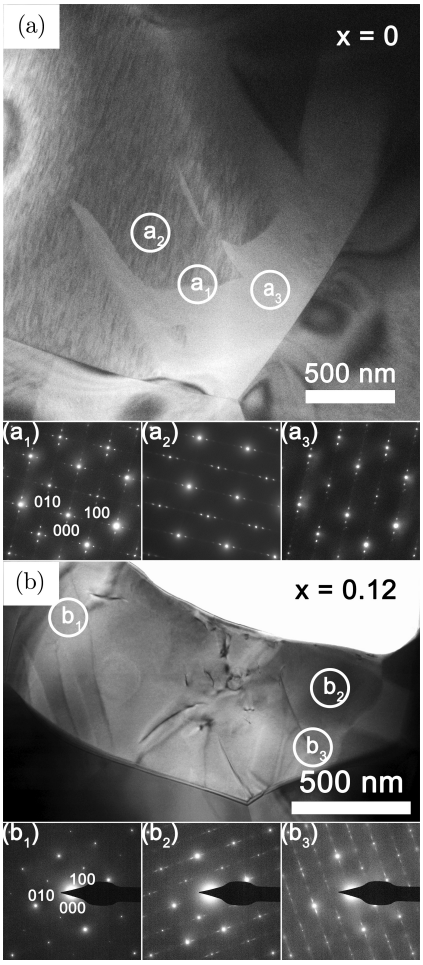

Fig. 4. TEM analysis of domain structures in grains along the $[001]_c$ zone-axis in ceramics of (a) $x = 0$ and (b) $x = 0.12$. The marked areas a_1, a_2, a_3 and b_1, b_2, b_3 are used to form the corresponding selected area electron diffraction patterns.

In the $x = 0.12$ composition, the grain size is notably smaller, consistent with the SEM observation. In the area b_1 of the $[001]_c$-oriented grain, two lamellar domains are identified but no satellite diffraction spots are observed in the reciprocal space. These domains could possibly be AFE domains without incommensurate modulations.[45] At the same time, numerous dislocations are observed in this grain, which can be attributed to the incompatible strain generated during sintering. Akin to $x = 0$, the checkerboard AFE domains are also present on the right side of the grain marked as b_2 and b_3.[46] The corresponding diffraction patterns exhibit streaking satellite spots that are much weaker in intensity, indicating a disrupted long-range AFE order. As a consequence of diffuse and elongated satellite spots, n varies continuously in a range. This range is 5.24–9.82 for the diffraction pattern in Fig. 4(b_2), and 4.88–11.55 for Fig. 4(b_3).

3.2. *Ferroelectric properties*

The polarization versus electric field hysteresis loops of LB100x ceramics are shown in Fig. 5, with recoverable energy density W_{rec} and energy efficiency η displayed. These dielectric energy storage properties are also listed in Table 1. The energy efficiency of all the compositions is above 90%, and when $x \leq 0.12$ the recoverable energy density is higher than 3.2 J/cm^3. With the increase of $(Li_{1/2}Bi_{1/2})$-substitution, the polarization-field ($P-E$) loops evolve into slimmer shapes until the appearance of the impurity phase at high substitution $x = 0.16$. The existence of the impurity phase in composition $x = 0.16$ has a noticeable impact on the experimental measurement reproducibility, so only the most representative data is shown here. The composition of $x = 0.12$ exhibits excellent energy storage performance with an excellent W_{rec} of 3.22 J/cm^3, an ultrahigh η of 94.0% and a high breakdown strength of 210 kV/cm.

It is clear in Fig. 5 that as $(Li_{1/2}Bi_{1/2})$-substitution increases, the phase transition becomes diffuse and gradual. It gets harder to read the critical fields E_F and E_A directly from the $P-E$ loops. In this study, the derivative of P with respect to E is taken and the fields at the peak of dP/dE are assigned to be the critical fields. The as-determined E_F and E_A are plotted in Fig. 5(f). It appears that E_F first decreases then

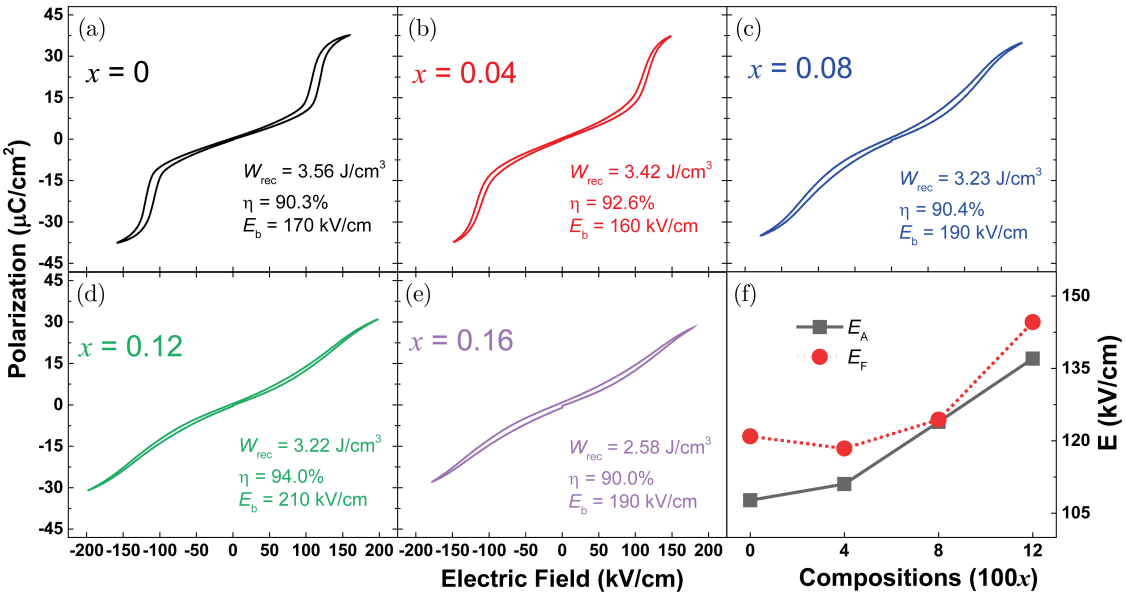

Fig. 5. Polarization *vs*. electric field hysteresis loops of LB100x series measured at 1 Hz at room temperature. (a) $x = 0$, (b) $x = 0.04$, (c) $x = 0.08$, (d) $x = 0.12$, (e) $x = 0.16$. (f) The critical fields (E_F for forward transition and E_A for reverse transition) are displayed for comparison.

increases while E_A exhibits a monotonic increase with the increase in substitution level. Close examinations on the P–E loops show that the electric hysteresis drops significantly, which confirms the enhanced relaxor characteristics of the material. The remanent polarization, assessed by the average of the positive and negative P-axis intercepts, is observed to be smaller than 1 μC/cm^2 for all compositions. Furthermore, the breakdown strength E_b (displayed in Fig. 5) is enhanced from 170 kV/cm in the base composition to 210 kV/cm in the composition of $x = 0.12$. The enhancement is believed to be originated primarily from the reduced grain size. These results indicate that the $(Li_{1/2}Bi_{1/2})$-substitution of Pb in $PbZrO_3$-based AFE compositions are beneficial to multiple dielectric energy-storage properties simultaneously.

3.3. *Dielectric properties*

The dielectric constant ε_r and loss tangent tan δ at 1 kHz as a function of temperature during heating are presented in Fig. 6. In the base composition, there are three anomalies in the ε_r versus T curve. The dielectric constant increases with temperature till reaching the peak value at 153°C, T_m, which is followed by a plateau region till 172°C. Presumably, the ceramic is in the AFE phase below T_m, and a multicell cubic phase in the plateau region, after which the ceramic is considered to be in the simple-cubic paraelectric (PE) phase. The multicell cubic plateau region only exists in the base composition, suggesting this intermediate phase is not stable in the compositions with $(Li_{1/2}Bi_{1/2})$-substitution.[19]

The maximum dielectric constant $\varepsilon_{m,r}$ at T_m gradually decreases with increase in Li^+ and Bi^{3+}, and T_m slightly shifts down to the low-temperature range (T_m is listed in

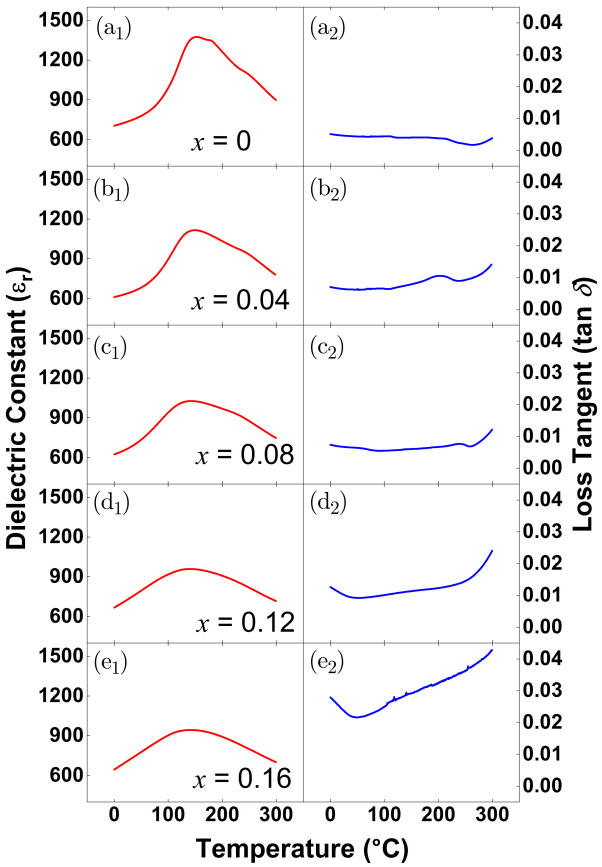

Fig. 6. Dielectric constant and loss tangent of LB100x composition series measured at 1 kHz during heating at 1°C/min. (a) $x = 0$, (b) $x = 0.04$, (c) $x = 0.08$, (d) $x = 0.12$, (e) $x = 0.16$.

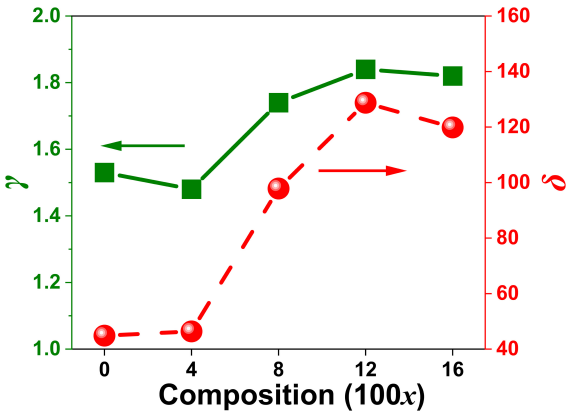

Fig. 7. The dielectric relaxation parameters γ and δ of the paraelectric phase in the LB100x composition series.

Table 1). The broadening of the dielectric peak at T_m suggests a diffused transition from AFE to PE and an enhanced dielectric relaxation. The relaxation characteristics can be quantitatively analyzed using the general Curie–Weiss law:[47,48]

$$\frac{\varepsilon_{m,r}}{\varepsilon_r} = 1 + \frac{(T - T_m)^\gamma}{2\delta^2}, \quad (6)$$

where γ is the degree of dielectric relaxation ($\gamma \in [1, 2]$, when $\gamma = 1$ the equation regresses into the Curie–Weiss law; $\gamma = 2$ represents a prototypical relaxor); δ is a parameter to describe the diffuseness of the phase transition at T_m. In this work, the data in the temperature range from $T_m + 40°C$ to $T_m + 140°C$ is fitted to Eq. (6). The fitting parameters are plotted in Fig. 7 and also listed in Table 1. The general trend is that the degree of the dielectric relaxation and the diffuseness of the phase transition substantially increase with the content of $(Li_{1/2}Bi_{1/2})$-substitution. This supports the introduced relaxor AFE behavior with reduced electric hysteresis and enhanced efficiency. The decrease in γ in $x = 0.04$ from the base composition may be attributed to the disappearance of the multicell cubic intermediate phase. The change in $x = 0.16$ is likely caused by the presence of the impurity phase.

4. Conclusions

With the aim of decreasing the sintering temperature, increasing the dielectric strength, reducing the electric hysteresis, boosting the energy-storage density and efficiency, a new AFE composition series, $[Pb_{0.93-x}La_{0.02}(Li_{1/2}Bi_{1/2})_x Sr_{0.04}][Zr_{0.57}Sn_{0.34}Ti_{0.09}]O_3$ with varying contents of $x = 0$, 0.04, 0.08, 0.12 and 0.16 is investigated. The $(Li_{1/2}Bi_{1/2})$-substitution of Pb in $PbZrO_3$-based AFE ceramics demonstrates multiple benefits. It is found that the sintering temperature can be reduced from 1350°C of the base composition $x = 0$–1075°C for $x = 0.12$ and 0.16 while maintaining a high relative density of $> 95\%$. Dielectric breakdown strength is also improved with $(Li_{1/2}Bi_{1/2})$-substitution. Due to the successful suppression of electric hysteresis, an ultrahigh energy efficiency (94.0%) is achieved in the composition of $x = 0.12$ at a recoverable energy density of 3.22 J/cm^3. These benefits are suggested to be originated from the prominent relaxor behavior imparted by the Li^+ and Bi^{3+} aliovalent dopants replacing Pb^{2+}.

Acknowledgments

This material is based upon the work supported by the U.S. Department of Energy's Office of Energy Efficiency and Renewable Energy (EERE) under the Advanced Manufacturing Office (AMO) Award Number DE-EE0009105.

ORCID

Binzhi Liu https://orcid.org/0000-0001-8293-3346
Anand P. S. Gaur https://orcid.org/0000-0003-1923-6876
Jun Cui https://orcid.org/0000-0001-7911-8172
Xiaoli Tan https://orcid.org/0000-0002-4182-663X

References

[1]R. Clarke, A. M. Glazer, F. W. Ainger, D. Appleby, N. J. Poole and S. G. Porter, Phase transitions in lead zirconate-titanate and their applications in thermal detectors, *Ferroelectrics* **11**, 359 (1976).
[2]K. Singh, Antiferroelectric lead zirconate, a material for energy storage, *Ferroelectrics* **94**, 433 (1989).
[3]W. Y. Pan, C. Q. Dam, Q. M. Zhang and L. E. Cross, Large displacement transducers based on electric field forced phase transitions in the tetragonal $(Pb_{0.97}La_{0.02})(Ti,Zr,Sn)O_3$ family of ceramics, *J. Appl. Phys.* **66**, 6014 (1989).
[4]B. Lu, P. Li, Z. Tang, Y. Yao, X. Gao, W. Kleemann and S.-G. Lu, Large electrocaloric effect in relaxor ferroelectric and antiferroelectric lanthanum doped lead zirconate titanate ceramics, *Sci. Rep.* **7**, 45335 (2017).
[5]S. Kwon, W. Hackenberger, E. Alberta, E. Furman and M. Lanagan, Nonlinear dielectric ceramics and their applications to capacitors and tunable dielectrics, *IEEE Electr. Insul. Mag.* **27**, 43 (2011).
[6]A. Chauhan, S. Patel, R. Vaish and C. R. Bowen, Anti-ferroelectric ceramics for high energy density capacitors, *Materials* **8**, 8009 (2015).
[7]Z. Liu, T. Lu, J. Ye, G. Wang, X. Dong, R. Withers and Y. Liu, Antiferroelectrics for energy storage applications: a review, *Adv. Mater. Technol.* **3**, 1800111 (2018).
[8]H. Shimizu, H. Guo, S. E. Reyes-Lillo, Y. Mizuno, K. M. Rabe and C. A. Randall, Lead-free antiferroelectric: xCaZrO$_3$-(1-x) NaNbO$_3$ system ($0 = x = 0.10$), *Dalton Trans.* **44**, 10763 (2015).
[9]Y. Tian, L. Jin, H. Zhang, Z. Xu, X. Wei, E. D. Politova, S. Yu. Stefanovich, N. V. Tarakina, I. Abrahams and H. Yan, High energy density in silver niobate ceramics, *J. Mater. Chem. A* **4**, 17279 (2016).
[10]J. Li, F. Li, Z. Xu and S. Zhang, Multilayer lead-free ceramic capacitors with ultrahigh energy density and efficiency, *Adv. Mater.* **30**, 1802155 (2018).

[11]F. Li, J. Zhai, B. Shen and H. Zeng, Recent progress of ecofriendly perovskite-type dielectric ceramics for energy storage applications, *J. Adv. Dielectr.* **08**, 1830005 (2018).
[12]J. Gao, Y. Zhang, L. Zhao, K.-Y. Lee, Q. Liu, A. Studer, M. Hinterstein, S. Zhang and J.-F. Li, Enhanced antiferroelectric phase stability in La-doped $AgNbO_3$: Perspectives from the microstructure to energy storage properties, *J. Mater. Chem. A* **7**, 2225 (2019).
[13]P. Fan, S.-T. Zhang, J. Xu, J. Zang, C. Samart, T. Zhang, H. Tan, D. Salamon, H. Zhang and G. Liu, Relaxor/antiferroelectric composites: A solution to achieve high energy storage performance in lead-free dielectric ceramics, *J. Mater. Chem. C* **8**, 5681 (2020).
[14]Z. Lu, D. Sun, G. Wang, J. Zhao, B. Zhang, D. Wang and I. Shyha, Energy storage properties in Nd-doped $AgNbTaO_3$ lead-free antiferroelectric ceramics with Nb-site vacancies, *J. Adv. Dielectr.* **13**, 2242006 (2023).
[15]R. Xu, J. Tian, Y. Feng, X. Wei and Z. Xu, Effects of Ti content on dielectric and energy storage properties of $(Pb_{0.94}La_{0.04})[(Zr_{0.70}Sn_{0.30})_{1-x}Ti_x]O_3$ ferroelectric/antiferroelectric ceramics, *J. Adv. Dielectr.* **06**, 1650033 (2016).
[16]A. Peláiz-Barranco, Y. Mendez-González, J. D. S. Guerra, X. Wang and T. Yang, Switching and energy-storage characteristics in PLZT 2/95/5 antiferroelectric ceramic system, *J. Adv. Dielectr.* **06**, 1620003 (2016).
[17]R. Xu, B. Li, J. Tian, Z. Xu, Y. Feng, X. Wei, D. Huang and L. Yang, $Pb_{0.94}La_{0.04}[(Zr_{0.70}Sn_{0.30})_{0.90}Ti_{0.10}]O_3$ antiferroelectric bulk ceramics for pulsed capacitors with high energy and power density, *Appl. Phys. Lett.* **110**, 142904 (2017).
[18]Z.-H. Niu, Y.-P. Jiang, X.-G. Tang, Q.-X. Liu and W.-H. Li, B-site non-stoichiometric $(Pb_{0.97}La_{0.02})(Zr_{0.95}Ti_{0.05})O_3$ antiferroelectric ceramics for energy storage, *J. Asian Ceram. Soc.* **6**, 240 (2018).
[19]P. Mohapatra, Z. Fan, J. Cui and X. Tan, Relaxor antiferroelectric ceramics with ultrahigh efficiency for energy storage applications, *J. Eur. Ceram. Soc.* **39**, 4735 (2019).
[20]R. Xu, Q. Zhu, Z. Xu, Y. Feng and X. Wei, PLZST antiferroelectric ceramics with promising energy storage and discharge performance for high power applications, *J. Am. Ceram. Soc.* **103**, 1831 (2020).
[21]X. Meng, Y. Zhao, Y. Li and X. Hao, Simultaneously achieving ultrahigh energy density and power density in $PbZrO_3$-based antiferroelectric ceramics with field-induced multistage phase transition, *J. Alloys Compd.* **868**, 159149 (2021).
[22]X. Meng, Y. Zhao, J. Zhu, L. Zhu, Y. Li and X. Hao, High energy-storage density and efficiency in $PbZrO_3$-based antiferroelectric multilayer ceramic capacitors, *J. Eur. Ceram. Soc.* **42**, 6493 (2022).
[23]J. Yoo, C. Lee, Y. Jeong, K. Chung, D. Lee and D. Paik, Microstructural and piezoelectric properties of low temperature sintering PMN-PZT ceramics with the amount of Li_2CO_3 addition, *Mater. Chem. Phys.* **90**, 386 (2005).
[24]K. Chung, J. Yoo, C. Lee, D. Lee, Y. Jeong and H. Lee, Microstructural, dielectric and piezoelectric properties of low-temperature sintering $Pb(Co_{1/2}W_{1/2})O_3$-$Pb(Mn_{1/2}Nb_{2/3})O_3$-$Pb(Zr,Ti)O_3$ ceramics with the addition of Li_2CO_3 and Bi_2O_3, *Sens. Actuator A Phys.* **125**, 340 (2006).
[25]V. Gil, J. Tartaj, C. Moure and P. Duran, Rapid densification by using Bi_2O_3 as an aid for sintering of gadolinia-doped ceria ceramics, *Ceram. Int.* **33**, 471 (2007).
[26]S. Le, J. Zhang, X. Zhu, J. Zhai and K. Sun, Sintering and electrochemical performance of Y_2O_3-doped barium zirconate with Bi_2O_3 as sintering aids, *J. Power Sources* **232**, 219 (2013).
[27]T. Kainz, B. Bitschnau, F. A. Mautner and K. Reichmann, Comparison of lanthanum and bismuth modification of lead zirconate-lead titanate PZT—a structural and dielectric study, *J. Eur. Ceram. Soc.* **36**, 507 (2016).
[28]T. Tunkasiri and G. Rujijanagul, Dielectric strength of fine grained barium titanate ceramics, *J. Mater. Sci. Lett.* **15**, 1767 (1996).
[29]B. Liu, X. Wang, R. Zhang and L. Li, Grain size effect and microstructure influence on the energy storage properties of fine-grained $BaTiO_3$-based ceramics, *J. Am. Ceram. Soc.* **100**, 3599 (2017).
[30]L. Yang, X. Kong, F. Li, H. Hao, Z. Cheng, H. Liu, J.-F. Li and S. Zhang, Perovskite lead-free dielectrics for energy storage applications, *Prog. Mater Sci.* **102**, 72 (2019).
[31]L. E. Cross, Relaxor ferroelectrics, *Ferroelectrics* **76**, 241 (1987).
[32]R. A. Cowley, S. N. Gvasaliya, S. G. Lushnikov, B. Roessli and G. M. Rotaru, Relaxing with relaxors: A review of relaxor ferroelectrics, *Adv. Phys.* **60**, 229 (2011).
[33]A. A. Bokov and Z.-G. Ye, Dielectric relaxation in relaxor ferroelectrics, *J. Adv. Dielectr.* **02**, 1241010 (2012).
[34]C. Ma and X. Tan, Phase diagram of unpoled lead-free (1-x)$(Bi_{1/2}Na_{1/2})TiO_3$–$xBaTiO_3$ ceramics, *Solid State Commun.* **150**, 1497 (2010).
[35]H. Qi, R. Zuo, A. Xie, A. Tian, J. Fu, Y. Zhang and S. Zhang, Ultrahigh energy-storage density in $NaNbO_3$-based lead-free relaxor antiferroelectric ceramics with nanoscale domains, *Adv. Funct. Mater.* **29**, 1903877 (2019).
[36]J. Chen, H. Qi and R. Zuo, Realizing stable relaxor antiferroelectric and superior energy storage properties in $(Na_{1-x/2}La_{x/2})(Nb_{1-x}Ti_x)O_3$ lead-free ceramics through A/B-site complex substitution, *ACS Appl. Mater. Interfaces* **12**, 32871 (2020).
[37]M. Zhou, R. Liang, Z. Zhou and X. Dong, Superior energy storage properties and excellent stability of novel $NaNbO_3$-based lead-free ceramics with A-site vacancy obtained via a Bi_2O_3 substitution strategy, *J. Mater. Chem. A* **6**, 17896 (2018).
[38]B. Liu and X. Tan, Structure, ferroelectric, and dielectric properties of $(Na_{1-2x}Ca_x)NbO_3$ ceramics, *J. Mater. Res.* **36**, 1076 (2021).
[39]D. Viehland, D. Forst, Z. Xu and J.-F. Li, Incommensurately modulated polar structures in antiferroelectric Sn-modified lead zirconate titanate: the modulated structure and its influences on electrically induced polarizations and strains, *J. Am. Ceram. Soc.* **78**, 2101 (1995).
[40]M.-J. Pan, S.-E. Park, K. A. Markowski, W. S. Hackenberger, S. Yoshikawa and L. E. Cross, Electric field induced phase transition in lead lanthanum stannate zirconate titanate (PLSnZT) antiferroelectrics: tailoring properties through compositional modification, *Ferroelectrics* **215**, 153 (1998).
[41]Y. Feng, Z. Xu, H. Li and X. Yao, Effect of La modifier on the electric hysteresis of lead zirconate stannate titanate compounds, *Ceram. Int.* **30**, 1393 (2004).
[42]L. Wang, Q. Li, L. Xue and X. Liang, Effect of Ti^{4+}:Sn^{4+} ratio on the phase transition and electric properties of PLZST antiferroelectric ceramics, *J. Mater. Sci.* **42**, 7397 (2007).
[43]R. D. Shannon, Revised effective ionic radii and systematic studies of interatomic distances in halides and chalcogenides, *Acta Crystallogr. A* **32**, 751 (1976).

[44]D. Viehland, X. H. Dai, J. F. Li and Z. Xu, Effects of quenched disorder on La-modified lead zirconate titanate: long-and short-range ordered structurally incommensurate phases, and glassy polar clusters, *J. Appl. Phys.* **84**, 458 (1998).
[45]Z. Fan, T. Ma, J. Wei, T. Yang, L. Zhou and X. Tan, TEM investigation of the domain structure in $PbHfO_3$ and $PbZrO_3$ antiferroelectric perovskites, *J. Mater. Sci.* **55**, 4953 (2020).
[46]B. Liu, L. Li, S.-T. Zhang, L. Zhou and X. Tan, In situ TEM observation on the ferroelectric-antiferroelectric transition in Pb(Nb,Zr,Sn,Ti)O_3/ZnO, *J. Am. Ceram. Soc.* **105**, 794 (2022).
[47]C. A. Randall, A. S. Bhalla, T. R. Shrout and L. E. Cross, Classification and consequences of complex lead perovskite ferroelectrics with regard to B-site cation order, *J. Mater. Res.* **5**, 829 (1990).
[48]B. S. Kang and S. K. Choi, Diffuse dielectric anomaly of $BaTiO_3$ in the temperature range of 400-700°C, *Solid State Commun.* **121**, 441 (2002).